Computation of Turbulent Free-Surface Flows Around Ships and Floating Bodies

Rodrigo Azcueta , MTG-Marinetechnik GmbH[1]

1 Introduction

In this work the commercial RANSE (Reynolds averaged Navier-Stokes equations) solver COMET was extended to both include the ship's running attitude in the calculations, and to simulate the motions of ships floating at the free surface. The work was presented as a PhD thesis, (*Azcueta (2001)*, pdf file can be sent on request). This paper summaries a part of it.

RANSE computations are increasingly being used to predict the ship resistance. In recent years the deformation of the free-surface and hence the wave-making resistance have been successfully implemented and validated. But to date the ship's running attitude, i.e. the dynamic sinkage and trim (and possibly heel) of the ship underway, has been neglected, even in research applications. All viscous flow computations known to me are to date in the *model-fixed* condition, either at the floating attitude at rest or at the running attitude measured in the towing tank. To improve the resistance predictions further, the ship's running attitude has to be included in the computations (*model-free* condition), since its effect is usually significant. This was the first aim of this work. The second was to extend the numerical method to simulate the motions of bodies floating freely at the free surface in the 6 DOF. An important requirement was to implement the coupling of the body motions and the fluid flow in such a way that both types of simulations – steady and unsteady – could be performed with the same program, and that the method be extensible to still more complex tasks, such as for ship maneuvering and ships in waves.

2 Numerical Method

To simulate the motions of bodies floating freely at the free surface, the equations of motion of the rigid body for the six degrees of freedom (6-DOF) can be solved together with the RANS equations. The general idea is to decouple the problem in the following way: the RANSE solver computes the flow around the body in the usual way, taking into account the fluid viscosity, flow turbulence and deformation of the free surface. The forces and moments acting on the body are then calculated by integrating the normal (pressure) and tangential (friction) stresses over the body surface. Following this, the 6-DOF equations can be solved using these forces and moments as input data, and the motion accelerations, velocities and displacements (translations and rotations) are obtained by integrating in time. The position of the body is then updated and the fluid flow is computed again for the new position. By iterating this procedure over the time, the body trajectory is obtained.

In this work a single-grid strategy was used for implementing the idea above, making use of the moving grid feature of the flow solver, where the rigid, body-fixed grid moves relative to an inertial frame of reference (observer fixed in space) and the fictitious flow forces are automatically taken into account in the flow equations. The equations of motion of the rigid body were implemented into the framework of the flow solver package COMET as a user-programmed module, linked and run simultaneously with the flow solver. The rigid body module can thus operate and update all flow variables, boundary conditions, and parameters of the numerical method needed to properly couple the fluid flow with the rigid body motions. The single grid extends over the entire computational domain. This approach can be easily extended to a two-grid system (inner block fixed to the moving body and outer block fixed to the earth) with a sliding interface between the blocks, in order to improve grid resolution and thus the quality of results. However, the single-grid approach proved so far to be very robust and yielded acceptable results. It also satisfied the requirement of working well

[1]Wandsbeker Königstr. 62, D 22401 Hamburg, Germany, Azcueta@MTG-Marinetechnik.de

for both types of problems, the computation of the steady-state running attitude of the ship and the time-accurate simulation of ship motions.

2.1 Outline of the RANSE solver

The starting point for the computation of incompressible viscous fluid flows are the RANS equations, i.e. the mass and momentum conservation equations, in conjunction with the standard k-ε model. Since in my approach the grid is forced to move with respect to the space-fixed frame of reference in which the RANS equations are expressed, the space-conservation law, which describes the conservation of volume when the CVs change their shape or position with time, must also be considered. This equation ensures that the sum of the volume fluxes through all the faces of a CV due to their movement is equal to the rate of change of the volume.

The solution domain is first subdivided into a finite number of non-overlapping CVs, which can basically be of any shape and have an arbitrary number of faces; for accuracy reasons, hexahedral CVs are used whenever possible. The grid can be locally refined by subdividing existing CVs. Also, grid blocks of different fineness and topology can be "glued" together and the grids do not have to match at the interface. Grid blocks are also allowed to slide at their interface.

A Finite-Volume Method (FVM) is used to discretize the conservation equations. For each CV, one algebraic equation is then obtained; each of these equations involves the unknown from the CV-center and from all neighboring CVs with which the current CV has common faces. Since the equations are non-linear, they have to be linearized to be solved iteratively. The equations are also coupled but are solved in a segregated manner, i.e. for each variable in turn, whereby other variables are treated as known by using the best update available from a previous iteration. In the course of obtaining an algebraic equation for each CV, three levels of approximation are applied:

- The integrals over surface, volume, and time are evaluated using midpoint-rule approximations, which use the value of the integrand at the center of the integration domain.

- Since the variable values are calculated at CV centers only, values at cell-face centers required for the evaluation of integrals have to be obtained by interpolation; here, linear interpolation is used, except on very coarse grids, where linear interpolation is blended with an upwind-biased approximation.

- In order to evaluate stress terms (forces) at CV-faces, numerical differentiation is needed to compute derivatives of the Cartesian velocity components with respect to Cartesian coordinates. This is done using either the Gauss method or polynomial fitting and central differences. The time derivative at the current time level is computed by differentiating a parabola fit through values at the current and two previous time levels; the time integration interval is centered around the current time level (a fully implicit scheme).

All of the above mentioned approximations are nominally of second order. The deferred-correction approach is used to reduce the implicit part of the discretized equations to the nearest neighbors only; the difference between the simplified and the full approximations is included on the right-hand side of the algebraic equations. This makes the matrix of the algebraic equation system positive definite with diagonal dominance which allows the use of simpler iterative solvers; here, conjugate-gradient type solvers are used (ICCG for symmetric and Bi-CGSTAB, for non-symmetric matrices). The mass conservation equation is transformed into a pressure-correction equation following the well-known SIMPLE-algorithm for colocated arrangements of variables.

For turbulent flows, the standard k-ε model with wall functions is used. The additional transport equations introduced by the model for the turbulent kinetic energy k and its dissipation rate ε have a similar form to that of the momentum equations and can be discretized and solved using the same principles. With k and ε the eddy viscosity μ_t can be determined.

Computations of three-dimensional flows with free surfaces – specially when they are unsteady, as is the case of freely-floating bodies – require considerable memory and computing time and are best performed on parallel computers. COMET is parallelized by domain decomposition in both space and time and can use either PVM or MPI message-passing libraries for communication between the processors. Both clusters of workstations and massive parallel computers can be used – as long as they support PVM or MPI standards.

An interface-capturing method of VOF type (called here volume-fraction method) is used to compute the deformation of the free surface. It is well suited to solve the kind of problems like those involving breaking waves, sprays, water jets, large amplitude ship motions, complex geometries like bulbous bow ships, etc. The advantages of this method were shown for breaking waves in *Azcueta et al. (1999a,b)*. In this method, the solution domain covers both the water and air region around the hull; both fluids are considered as an effective fluid with variable properties, which are determined at any spatial location according to the volume fraction of one constituent fluid (e.g. water). The volume fraction c is obtained by solving the corresponding conservation equation. The discretization of this equation requires special attention. Higher-order schemes violate the boundedness requirement, which requires that $0 \leq c \leq 1$; on the other hand, numerical diffusion of low-order schemes must be avoided in order to retain the interface between the two fluids as sharp as possible. Here, the high-resolution interface-capturing scheme (HRIC) is used, which computes the cell-face value of c as a blend of upwind and downwind interpolation, *Muzaferija and Perić (1998)*. The choice of the blending factor depends on the local distribution of the volume fraction, relative position of the free surface to the cell face, and the local value of the Courant number. The Courant number indicates how much of one fluid is available in the donor cell and the scheme is tuned in such a way that no more fluid can drain out of one CV within one time step than was available in it. Another important factor is the orientation of the interface relative to the CV-face. The normal to the interface – which is assumed to lie where the volume fraction has the value $c = 0.5$ – is obtained by computing the gradient of c; it is equal to zero everywhere except in the interface region. With this approach, the interface is usually smeared across two to three cells. If one CV is partially filled with one and partially with the other fluid, it is assumed that both fluids have the same velocity and pressure. The free surface does not represent a boundary and no boundary conditions need to be prescribed at it. If surface tension is significant at the free surface, this can also be taken into account by transforming the resulting surface-tension force into a body force.

2.2 Coupling fluid flow and rigid body motion

Two orthogonal right-handed Cartesian coordinate systems are used:

1. A non-rotating, non-accelerating frame of reference O, X, Y, Z which moves forward with the mean ship speed. This frame of reference is a Newtonian reference system in which the equations of linear and angular momentum are valid. The undisturbed free-surface plane always remains parallel to the XY plane. The Z-axis points upwards. The position and orientation of the body at any point in time is described with respect to this reference system (RS). The unit vectors defining this RS are denoted by $\vec{I}$, $\vec{J}$ and $\vec{K}$.

2. A body-fixed frame of reference G, x, y, z with origin at the center of mass of the body. The unit vectors defining this RS are $\vec{i}$, $\vec{j}$ and $\vec{k}$. The computational grid always remains attached to this RS as it moves. Following the common practice in ship flow calculations, the x-axis is directed in the main flow direction, i.e. from bow to stern, the y-axis is taken positive to starboard and the z-axis is positive upwards.

The motion of the rigid body in the 6-DOF are determined by integrating the equations of variation of linear and angular momentum. The equation of variation of linear momentum in the form referred to the center of gravity is:

$$m\ddot{\vec{X}}_G = \vec{F} \tag{1}$$

m is the body mass, $\ddot{\vec{X}}_G$ the absolute linear acceleration of G (i.e. in Newtonian RS), and $\vec{F}$ the total force acting on the body expressed in the Newtonian RS. The contributions to the total force are:

$$\vec{F} = \vec{F}_{flow} + \vec{W} + \vec{F}_{ext} \tag{2}$$

$\vec{F}_{flow}$ is the total fluid force determined by integrating the pressure field and viscous stresses, obtained from the RANSE solver, discretized over the body as:

$$\vec{F}_{flow} = \sum_{j=1}^{n} (-p_j \vec{n}_j + \vec{\tau}_j) S_j \tag{3}$$

The subscript j stands for each CV face defining the body surface. p is the pressure, $\vec{n}$ the normal vector to each CV face (components in Newtonian RS), $\vec{\tau}$ the tangential viscous wall shear stress acting on each CV face (components in Newtonian RS), and S the CV face area. $\vec{F}_{flow}$ includes the static and dynamic components for the water and air flow. When the air contribution is negligible, only the hydrostatic and hydrodynamic components are taken into account. $\vec{W}$ is the body weight force, i.e. $\vec{W} = m\vec{g}$, where $\vec{g}$ is the acceleration of gravity acting in the negative Z-direction. $\vec{F}_{ext}$ can be any external force acting on the body which one wants to introduce to simulate for instance propeller and rudder forces, the towing force, sail forces, etc. In the 3-D simulations of this work (resistance tests), only the towing force $\vec{F}_{tow}$ was considered. The towing force attachment point $\vec{X}_{tow}$ has to be known.

The equation of variation of angular momentum in the form referred to the center of gravity is:

$$\overline{\overline{T}}\,\overline{\overline{I}}_G \overline{\overline{T}}^{-1} \dot{\vec{\Omega}} + \vec{\Omega} \times \overline{\overline{T}}\,\overline{\overline{I}}_G \overline{\overline{T}}^{-1} \vec{\Omega} = \vec{M}_G \tag{4}$$

$\dot{\vec{\Omega}}$ and $\vec{\Omega}$ are the absolute angular acceleration and angular velocity (i.e. in Newtonian RS), respectively, and $\vec{M}_G$ is the total moment with respect to G expressed in the Newtonian RS. $\overline{\overline{I}}_G$ is the tensor of inertia of the body about the (G, x, y, z) axes (constant with respect to the body-fixed RS):

$$\overline{\overline{I}}_G = \begin{bmatrix} I_{xx_G} & -I_{xy_G} & -I_{xz_G} \\ -I_{yx_G} & I_{yy_G} & -I_{yz_G} \\ -I_{zx_G} & -I_{zy_G} & I_{zz_G} \end{bmatrix} \tag{5}$$

I_{xx_G} is the roll moment of inertia of the ship about the Gx axis:

$$I_{xx_G} = \int_B (y^2 + z^2)\, dm \tag{6}$$

and analogous for the pitch I_{yy_G} and yaw I_{zz_G} moments of inertia (B stands for the whole body mass). I_{xy_G}, I_{xz_G} and I_{yz_G} are the product of inertia (note that $I_{xy_G} = I_{yx_G}$, $I_{xz_G} = I_{zx_G}$, $I_{yz_G} = I_{zy_G}$):

$$I_{xz_G} = \int_B xz\, dm \tag{7}$$

$\overline{\overline{T}}$ in Eq.(4) is the transformation matrix from the body-fixed into the Newtonian RS. The columns of $\overline{\overline{T}}$ are the unit vectors attached to the body-fixed RS, i.e. $\vec{i}$, $\vec{j}$ and $\vec{k}$. The absolute time derivative of the unit vectors, used to find the new orientation of the body, are:

$$\dot{\vec{i}} = \vec{\Omega} \times \vec{i} \quad , \quad \dot{\vec{j}} = \vec{\Omega} \times \vec{j} \quad , \quad \dot{\vec{k}} = \vec{\Omega} \times \vec{k} \tag{8}$$

The contributions to the total moment acting on G, expressed in terms of the Newtonian RS, are:

$$\vec{M}_G = \vec{M}_{G_{flow}} + (\vec{X}_{tow} - \vec{X}_G) \times \vec{F}_{ext} \tag{9}$$

$\vec{M}_{G_{flow}}$ is the total fluid flow moment, discretized as:

$$\vec{M}_{G_{flow}} = \sum_{j=1}^{n} (\vec{X}_j - \vec{X}_G) \times (-p_j \vec{n}_j + \vec{\tau}_j) S_j \tag{10}$$

$\vec{X}_j$ are the position vectors of the CV face centers expressed in the Newtonian RS for all faces defining the body. The towing force $\vec{F}_{tow}$ was considered in the 3-D simulations as an external force creating a moment.

The body motions are described in each time instant by the position of its center of gravity $\vec{X}_G$ and the body orientation given by $\overline{\overline{T}}$. For ship motions, the displacements of the center of mass in two successive time instants are defined in terms of the Newtonian RS as:

Surge:	$\Delta X_G = {X_G}^{t_{n+1}} - {X_G}^{t_n}$	(translation along $\vec{I}$)
Sway:	$\Delta Y_G = {Y_G}^{t_{n+1}} - {Y_G}^{t_n}$	(translation along $\vec{J}$)
Heave (sinkage):	$\Delta Z_G = {Z_G}^{t_{n+1}} - {Z_G}^{t_n}$	(translation along $\vec{K}$)

The superscript t_{n+1} stands for the actual time instant and t_n for the previous time instant, for which the fluid field is known.

The new position of G in each time step is found by integrating in time the equation of variation of linear momentum, Eq.(1). After the first integration the velocity of G for the new time instant can be determined as:

$$\dot{\vec{X}}_G^{\,t_{n+1}} = \dot{\vec{X}}_G^{\,t_n} + \frac{\Delta t}{m} \tilde{\vec{F}} \tag{11}$$

Δt is the size of the time step in seconds and $\tilde{\vec{F}}$ is a general expression for the force acting on the body used for the time integration (mean value over the integration interval). After a second integration the position of G for the new time instant can be determined as:

$$\vec{X}_G^{\,t_{n+1}} = \vec{X}_G^{\,t_n} + \Delta t \; \tilde{\dot{\vec{X}}}_G \tag{12}$$

$\tilde{\dot{\vec{X}}}_G$ is a general expression for the body velocity used for the time integration. Depending on how $\tilde{\vec{F}}$ and $\tilde{\dot{\vec{X}}}_G$ are approximated, different discretization methods can be constructed. A first-order explicit method in the form

$$\tilde{\vec{F}} = 0.5 \; (\vec{F}^{t_n} + \vec{F}^{t_{n-1}}) \quad , \quad \tilde{\dot{\vec{X}}}_G = 0.5 \; (\dot{\vec{X}}_G^{\,t_n} + \dot{\vec{X}}_G^{\,t_{n+1}}) \tag{13}$$

was very stable and preferably used. This proposed integration method is a mixture of a trapezoid rule using the known forces in the last two time instants to obtain the new velocity and a Crank-Nicholson method for the integration of the velocity to obtain the position of the body. Since other explicit methods except for the proposed one behave very unstable in the case of large flow induced accelerations, and since the time steps needed for computing the deformation of the free surface have to be chosen very small anyway, it was considered that the proposed method was a good choice for the small time steps used in the simulations. As we will see in one example of the application of the method (time-accurate simulation of a drop test), the proposed discretization delivered acceptable simulated motions.

The new orientation of the body in each time step is found by integrating the equation of variation of angular momentum, Eq.(4). Using the same proposed integration method as described above for the linear motions, and after the first integration the angular velocity for the new time instant $\vec{\Omega}^{t_{n+1}}$ is obtained. Instead of integrating again $\vec{\Omega}^{t_{n+1}}$ to obtain the rotation angles of the body, I preferred to determine the new orientation of the body in a generalized way by integrating the unit vectors of the body-fixed RS, which are the components of the transformation matrix. Eq.(8) only needs to be integrated for two of the three unit vectors, e.g. to obtain $\vec{i}^{\,t_{n+1}}$:

$$\vec{i}^{\,t_{n+1}} = \vec{i}^{\,t_n} + \Delta t \; 0.5 \; (\vec{\Omega}^{t_{n+1}} + \vec{\Omega}^{t_n}) \times \vec{i}^{\,t_n} \tag{14}$$

and analogous for $\vec{j}^{\,t_{n+1}}$. The third unit vector, in this case $\vec{k}$, is determined for the new time instant with:

$$\vec{k}^{\,t_{n+1}} = \vec{i}^{\,t_{n+1}} \times \vec{j}^{\,t_{n+1}} \tag{15}$$

Following this, the new triad $(\vec{i}^{\,t_{n+1}}, \vec{j}^{\,t_{n+1}}, \vec{k}^{\,t_{n+1}})$ is ortho-normalized in the usual way.

After integrating the equations of variation of linear and angular momentum once and before proceeding with the second integration, the linear and angular velocities at the new time instant are modified in the following cases and with following purposes:

1. Only when the transient characteristic of the motion is not important (e.g. when marching toward a steady-state solution), the convergence towards the final state can be improved by retarding the body velocity with:

$$\dot{\vec{X}}_G^{\,*t_{n+1}} = \dot{\vec{X}}_G^{t_{n+1}}\ DF \quad , \quad \vec{\Omega}^{\,*t_{n+1}} = \vec{\Omega}^{t_{n+1}}\ DF \tag{16}$$

   The delay factor DF is a factor between 0 and 1. The effects of retarding the velocities with DF will be analyzed in detail in the application examples.

2. The motions are constrained in the directions in which the ship is kept fixed, e.g. the surge motion with:

$$\dot{X}_G^{*t_{n+1}} = \dot{X}_G^{t_n} \tag{17}$$

   In this way, if set to zero for t_0, it will remain zero throughout the simulation. Also the timing with which the different DOF are released is handled after obtaining the new velocities. The timing for releasing the DOF is important for instance to accelerate convergence or to analyze the effects of the different DOF on resistance in the case of steady-state flows. To simulate transient body motions, all DOF obviously have to be released at the same time. Moreover, the body velocity should not be retarded. More details about this are found in the application examples.

From the generalized body orientation at the new time instant given by $\overline{\overline{T}}^{t_{n+1}}$, one is interested in obtaining the angles of rotation of the body for two purposes: 1. To determine the variation of the angles with respect to the last time step for rotating the body from the last into the new position; 2. To determine the absolute angles with respect to the Newtonian RS for monitoring the results of the rotation. The calculation of the angles of rotation demands special care. The order of the rotation has to be defined to be unequivocal. There is more than only one possible definition for the order of rotation, but the following seems to be the most appropriate one for seakeeping and maneuvering problems as well as for the ship's trim and sinkage. Starting from the old body orientation and after G was displaced to the new position $(G^{t_{n+1}}, \vec{i}^{\,t_n}, \vec{j}^{\,t_n}, \vec{k}^{\,t_n})$, the three rotations $\delta\psi$, $\delta\theta$ and $\delta\phi$ for two successive time instants are executed in the following order, Fig.1:

1. The first rotation $\delta\psi$ is around the vertical axis in the body-fixed RS (G, x, y, z), i.e. around $\vec{k}^{\,t_n}$. The RS has changed now to $(G^{t_{n+1}}, \vec{i}^{aux}, \vec{j}^{aux}, \vec{k}^{\,t_n})$. $\vec{i}^{aux}$ and $\vec{j}^{aux}$ are the normalized unit vectors of the projection of $\vec{i}^{t_{n+1}}$ and $\vec{j}^{t_{n+1}}$ onto the $\vec{i}^{\,t_n}\vec{j}^{\,t_n}$ plane.

2. The second rotation $\delta\theta$ is around the new transverse axis, i.e. around $\vec{j}^{aux}$. The RS has changed now to $(G^{t_{n+1}}, \vec{i}^{t_{n+1}}, \vec{j}^{aux}, \vec{k}^{aux})$.

3. The last rotation $\delta\varphi$ is around the new longitudinal axis, i.e. around $\vec{i}^{t_{n+1}}$. The RS has finally become $(G^{t_{n+1}}, \vec{i}^{t_{n+1}}, \vec{j}^{t_{n+1}}, \vec{k}^{t_{n+1}})$.

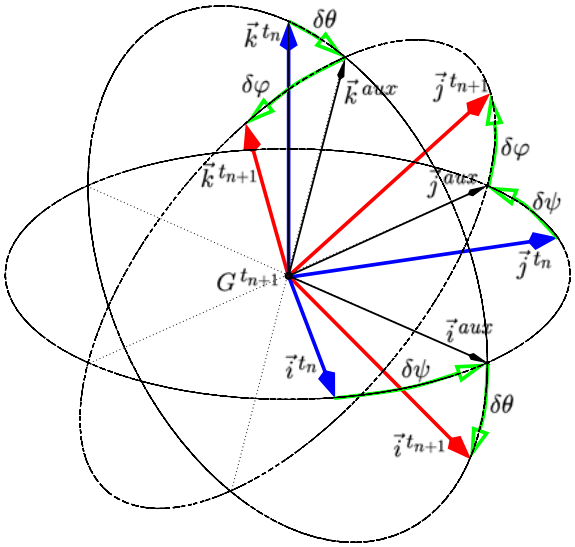

Fig.1: Definition of the rotation angles $\delta\varphi, \delta\theta, \delta\psi$

The equations prescribing the rotations as defined above are:

$$\vec{i}^{\,aux} = \frac{\vec{i}^{\,t_{n+1}} - (\vec{i}^{\,t_{n+1}} \cdot \vec{k}^{\,t_n})\vec{k}^{\,t_n}}{|\vec{i}^{\,t_{n+1}} - (\vec{i}^{\,t_{n+1}} \cdot \vec{k}^{\,t_n})\vec{k}^{\,t_n}|}, \qquad \vec{j}^{\,aux} = \vec{k}^{\,t_n} \times \vec{i}^{\,aux} \tag{18}$$

$$\delta\psi^{\,t_{n+1}} = \arcsin[(\vec{i}^{\,t_n} \times \vec{i}^{\,aux}) \cdot \vec{k}^{\,t_n})] \tag{19}$$

$$\delta\theta^{\,t_{n+1}} = \arcsin[(\vec{i}^{\,aux} \times \vec{i}^{\,t_{n+1}}) \cdot \vec{j}^{\,aux})] \tag{20}$$

$$\delta\varphi^{\,t_{n+1}} = \arcsin[(\vec{j}^{\,aux} \times \vec{j}^{\,t_{n+1}}) \cdot \vec{i}^{\,t_{n+1}})] \tag{21}$$

The absolute rotations with respect to the Newtonian RS are:

Yaw (drift) angle:	$\Delta\psi^{\,t_{n+1}} = \psi^{\,t_{n+1}}$	(rotation around $\vec{K}$)
Pitch (trim) angle:	$\Delta\theta^{\,t_{n+1}} = \theta^{\,t_{n+1}}$	(rotation around $\vec{j}^{\,aux}$)
Roll (heel) angle:	$\Delta\varphi^{\,t_{n+1}} = \varphi^{\,t_{n+1}}$	(rotation around $\vec{i}^{\,t_{n+1}}$)

They are calculated using the same equations above but replacing $\vec{k}^{\,t_n}$ and $\vec{i}^{\,t_n}$ with $\vec{K}$ and $\vec{I}$, respectively.

The no-slip boundary condition at the body wall implies that the velocity of any point on the hull surface and the fluid velocity must be identical. Since the body is translating and rotating with respect to the main direction of the flow, the motion velocities have to be imposed at each CV face defining the body as boundary condition. For this purpose the equation of the state of velocities is used, which expresses the velocity of any point of the rigid body as a function of the velocity of a reference point – in this case of G – and the angular velocity of the body:

$$\dot{\vec{X}}_j = \dot{\vec{X}}_G + \vec{\Omega} \times \left(\vec{X}_j - \vec{X}_G\right) \tag{22}$$

Since the flow solver needs all variables expressed in terms of the Newtonian RS, Eq.(22) is also expressed in terms of the Newtonian RS.

To set the boundary conditions at the external boundaries when using the single-grid strategy requires special attention. In all CV faces at the boundaries which are crossed by the undisturbed free-surface plane an interpolated value (between 0 and 1) for the volume fraction have to be set. In this way, the CVs at the external boundaries have no restriction in size and the transition from water to air at the free surface is smooth. The volume fraction distribution is updated every time step as the grid moves with respect to the undisturbed free-surface plane, which is fixed in space. An accurate

interpolation of the volume fraction is performed at every time step by a procedure which calculates the truncated areas (and volumes) of arbitrary shaped CVs. This interpolation is not only used to set the boundary conditions at every time step but also to accurately initialize the volume fraction field in the whole computational domain in order to accelerate the convergence at the beginning of the computation.

3 Computation of the ship's trim and sinkage

3.1 Series 60 hull

The Series 60 $C_B = 0.6$ has become a benchmark for oblique flow calculations due to the detailed measurements available from the University of Iowa, *Longo and Stern (1996)*. The calculations in this work were performed for the Froude number $F_n = 0.316$, for the straight-ahead condition and for the smallest measured drift angle ($\beta = 2.5°$). In the first case, the flow and wave pattern are symmetric, and only dynamic sinkage and trim were calculated, while in the second case the heel angle was calculated as well. The computations were performed on a coarse grid with $38,912$ CVs. The lateral boundary conditions (top, sides and bottom) were set as an inlet condition, so that flow velocity, turbulent parameters and the volume fraction are specified there as well.

The position of the center of gravity greatly influences the calculated final running attitude; the longitudinal position X_G determines the trim angle and the vertical position Z_G, the heel angle, as well as to some extent the trim angle. The moments of inertia of the model influence the convergence history, i.e. the transition from the initial steady-state to the final state. *Longo and Stern (1996)* unfortunately do not give the vertical position of G and the moments of inertia. X_G was determined from the balance of forces for the model on an even keel, i.e. at the start of the computation. Z_G was estimated with $\overline{KG} \approx 0.46 - 0.64D$, *Schneekluth (1988)*, where $\overline{KG}$ stands for the vertical distance between the ship keel and G, and D is the depth of the ship. The moments of inertia $I_{x_G} = \Delta {k_{x_G}}^2$ and $I_{z_G} \approx I_{y_G} = \Delta {k_{y_G}}^2$ were also estimated from *Schneekluth (1988)* with $k_{x_G} \approx 0.40B$ and $k_{y_G} \approx 0.26L$. Here, k_{x_G} and k_{y_G} are the roll and pitch radius of gyration about the ship-bounded axis passing through the center of gravity. The products of inertia were set equal to zero. The towing force attachment point also influences the converged trim and heel angles. The height of the towing force attachment point was $0.0128L$ above the design waterline, *Longo and Stern (1996)*.

Table I: Measured and calculated values in 0° drift condition

	C_F $[10^{-3}]$	C_P (C_R) $[10^{-3}]$	C_T $[10^{-3}]$	sinkage $[L]$	trim ang. $[°]$	wetted surf. $[L^2]$
A: exp. (free)	3.54	2.42	5.96	−0.00392	−0.100	0.1699
B: comp. (fixed)	3.19	1.90	5.09	0.00000	0.000	0.1701
C: comp. (free)	3.43	2.18	5.61	−0.00360	−0.094	0.1779
$(B-A)/A$	−9.9%	−21.5%	−14.6%	–	–	0.1%
$(C-A)/A$	−3.1%	−10.0%	−5.9%	−8.2%	−6.0%	+4.7%
$(C-B)/B$	+7.5%	+14.7%	+10.2%	–	–	+4.6%

Table I compares computed and measured results for 0° drift. Δt and the blending factor for the discretization of convective fluxes in the momentum equations influence the computed values, *Azcueta (2000)*. The results presented for $\Delta t = 0.005$ s and 80% CDS. The mixing ratio UDS-CDS was also varied in this investigation and its effects will be addressed below. Δt was kept constant, so that its effect does not influence the following results. Only one outer iteration per time step was performed (pseudo-steady time integration). For the model-free calculations, the CPU time needed per time step increases by about 50% compared to the model-fixed case. This is due to the transformation of the whole grid geometry into the new position after each time step, which is computationally very expensive, as well as to some extent due to the calculation of the forces and moments, integration of the equations of motion, more complicated boundary conditions, etc.

The C_F value from the experiment was determined from the ITTC'57 correlation line, while the

residual resistance coefficient is $C_R = C_T - C_F$. The experimental values are for the model-free condition. The resistance coefficients were normalized following the standard practice in towing tanks of using the wetted surface at rest. The computation under-predicts the measured total resistance coefficients by 14.6% in the model-fixed case and by 5.9% in the model-free case. The model-free calculation predicts the total resistance 10% larger than the model-fixed calculation and thus in closer agreement with the experiments. The computed wetted surface for the model-fixed condition with forward speed (with distortion of the free surface) is insignificantly larger than for the model at rest. However, for the model-free condition it is 4.7% larger, mostly due to the sinkage than to the trim or the deformation of the free surface in wave crests and troughs, whose contributions to the wetted surface cancel each other out. All computed resistance coefficients include the air resistance as simulated for the tank conditions. At this Reynolds number, it accounts on average for $1.5\% - 2.0\%$ of the total resistance. The sinkage in the calculations corresponds to a downward displacement of the center of gravity (negative sinkage), while in the experiments it is a measure of the average upward or downward deflection of the forward and aft perpendiculars. Since G is basically midships there is practically no difference between the two definitions. The computed sinkage under-predicts the measurements by about 8%. The trim angle definition is the same for both measurement and computation. A negative trim corresponds to a bow down and stern up attitude. The computed trim angle agrees well with the measurement.

In the second test condition – the steady-state drift flow at a small drift angle of 2.5° – the dynamic heel angle was also computed. For this test condition, the results are less satisfactory than for 0° drift. The main reason for this is that the asymmetric flow is basically more complicated than the parallel flow, with possible three-dimensional separation, wave breaking and vortex-free-surface interaction. The used grid is really too coarse to capture the asymmetric flow characteristics accurately. The measured total resistance increases by 4.5% with respect to the 0°–drift case. The computation under-predicts C_T by 6.1%. The gain in accuracy for C_T in the model-free condition (compared to the model-fixed condition) accounts for 8.3%, Table II.

Table II: Measured and calculated force coefficients for 2.5° drift

	C_F $[10^{-3}]$	C_P (C_R) $[10^{-3}]$	C_T $[10^{-3}]$	C_Y $[10^{-3}]$	C_M $[10^{-3}]$
A: exp. (free)	3.54	2.69	6.23	4.90	−0.33
B: comp. (fixed)	3.15	2.25	5.40	3.05	−0.35
C: comp. (free)	3.37	2.48	5.85	2.68	−0.37
$(B-A)/A$	−11.0%	−16.3%	−13.3%	−37.7%	+6.1%
$(C-A)/A$	−4.8%	−7.8%	−6.1%	−45.3%	+12.1%
$(C-B)/B$	+7.0%	+10.2%	+8.3%	−12.1%	+5.7%

The largest differences occur for the side force coefficient $C_Y = F_y/(0.5\rho v_o^2 S_o)$. F_y is the total side force in the ship-fixed reference system. The yaw moment coefficient $C_M = M_z/(0.5\rho v_o^2 L^3)$ is much better predicted than the side force. The free condition deteriorates the prediction of side force even more. The reason for this bad prediction is low grid resolution as well as an inappropriate turbulence model. Oblique flow computations by *Cura Hochbaum (1998)* suffered to some extent from similar problems, although he attributes the side force under-prediction to the lack of the free surface and the dynamic squat and heel. A negative drift angle ($\beta = -2.5°$) means in this case that the flow comes from the port side of the model. In the 2.5°–drift condition and according to the measurements, the sinkage increases by around 6% and the trim angle by 23%. The asymmetric flow induces a heel angle of 0.85° (measurement) towards the direction of the flow, that means in this case towards the port side. Table III shows the predicted sinkage, trim and heel angle for $\overline{KG} = 0.44D$ and the comparison with the measured values. The heel angle change considerably by choosing a different $\overline{KG}$ and thus $\overline{GM}$. For instance for $\overline{KG} = 0.47D$ the predicted heel angle becomes +15.3% larger and for $\overline{KG} = 0.41D$ it becomes −23.5% smaller than measured. This fact stresses the importance of a detailed documentation of the experimental set-up for CFD validation purposes.

Table III: Measured and calculated trim and sinkage for 2.5° drift

	sinkage $[L]$	trim ang. [°]	heel ang. [°]	wetted surf. $[L^2]$
A: exp. (free)	−0.00414	−0.123	0.85	0.1699
B: comp. (fixed)	0.00000	0.000	0.00	0.1700
C: comp. (free)	−0.00378	−0.140	0.80	0.1782
$(B-A)/A$	–	–	–	+0.4%
$(C-A)/A$	−8.7%	+13.8%	−5.9%	+4.9%
$(C-B)/B$	–	–	–	+4.9%

In general, the calculations with dynamic sinkage and trim and heel satisfactorily predicted the measured resistance and running attitude of the Series 60 model in both the straight-ahead and drift condition, and substantially improved the resistance prediction compared to the calculation in the model-fixed condition.

In the following, the convergence history of forces and motions will be analyzed in detail for the 0°–drift condition. All values mentioned in the next paragraphs and shown in the diagrams can be found also in Tables I to III. However, the resistance coefficients in the diagrams were normalized using the computed wetted surface underway while the coefficients in the tables were normalized using the wetted surface at rest. These calculations were performed varying the mixing ratio of UDS-CDS to study its influence on the pressure force, following *Azcueta (2000)*. This study demands a much greater computational effort than by just using a constant blending factor, but it gives insight into the convergence of predicted values. This in turn can help to accelerate convergence in future work.

Fig.2 (top left) shows the convergence history for the model-fixed condition. The first few seconds of the simulation display strong oscillations. This is due to the fact that the simulation was started with the ship advancing at full forward speed. Until 50 s, pure UDS was used. ¿From there on, UDS was blended with CDS in 10% and 10 s steps, until 80% CDS was reached and used for the last 20 s. The values presented in Tables I to III were averaged between these last 130 s to 140 s, i.e. for 80% CDS. The pressure resistance coefficient depends on the UDS-CDS mixing ratio. The pressure resistance coefficient is represented by the line which looks like stairs. The friction resistance coefficient depends on the blending factor only by a negligible amount. The trim moment displays a similar dependence like the pressure resistance. The trim angle for this case is zero. The heave force remains constant at 38.3 N. This value is the total vertical force computed. It contains the hydrostatic component for the fixed design draft Δ_o plus a hydrodynamic component (negative sign) also in the fixed condition. The difference from the model displacement $\Delta = -41.50$ N (normalized for 1 m model) is the force constrained in the simulation or being supported by the balance in the towing tank carriage.

Fig.2 (top right) shows the case where the model was allowed free sinkage. The sinkage is represented by the line which drops at 30 s to −0.0036 m. At the same time, the vertical force goes up and balances exactly the model displacement: $F_{z_{tot}} = \Delta_o + \delta\Delta + F_{z_{dyn}}$, so that hydrodynamic component $F_{z_{dyn}}$ equals the change in displacement $\delta\Delta$. The pressure resistance line shifts 9.5% upwards. The trim moment changes substantially, even changing the sign between 40% and 50% CDS.

Fig.2 (bottom), corresponds to the model-free (sinkage+trim) calculation. In general, the convergence lines in this case display more high-frequency oscillations. This may be due to the fact that the grid lines are less aligned to the flow than before, especially at the boundary region. Heave force, friction resistance and sinkage show the same behavior as in the case before. The pitch motion is released at 25 s simulation time. With pure UDS the hull trims nose up (squat). With ≈ 30% CDS, it is on an even keel. At 80% CDS, the hull is trimmed 0.1° nose down. The trim moment is in balance. It is not at zero but in this case ≈ 0.01 Nm, which corresponds to the trim moment caused by the towing force. By comparing with the sinkage-only case, one can calculate the trim moment caused by the towing force to be 22% of the total trim moment. The pressure resistance basically remained unchanged, although it oddly became 1% smaller in the trimmed condition.

The convergence histories for the 2.5°–drift condition (model also free to heel) show the same

behavior as for the 0°–drift condition. The heel moment and side force (in this case the lift, i.e. force in Y-direction) also show a strong dependence on the UDS-CDS ratio.

The wave patterns for both the 0°-drift and the 2.5°-drift model-free conditions look very similar to those in the model-fixed condition (will not be shown here), since sinkage, trim and heel are relatively small (deep water, moderate Froude number and drift angle). The next application case will show large changes in wave pattern due to large changes in running attitude of the model.

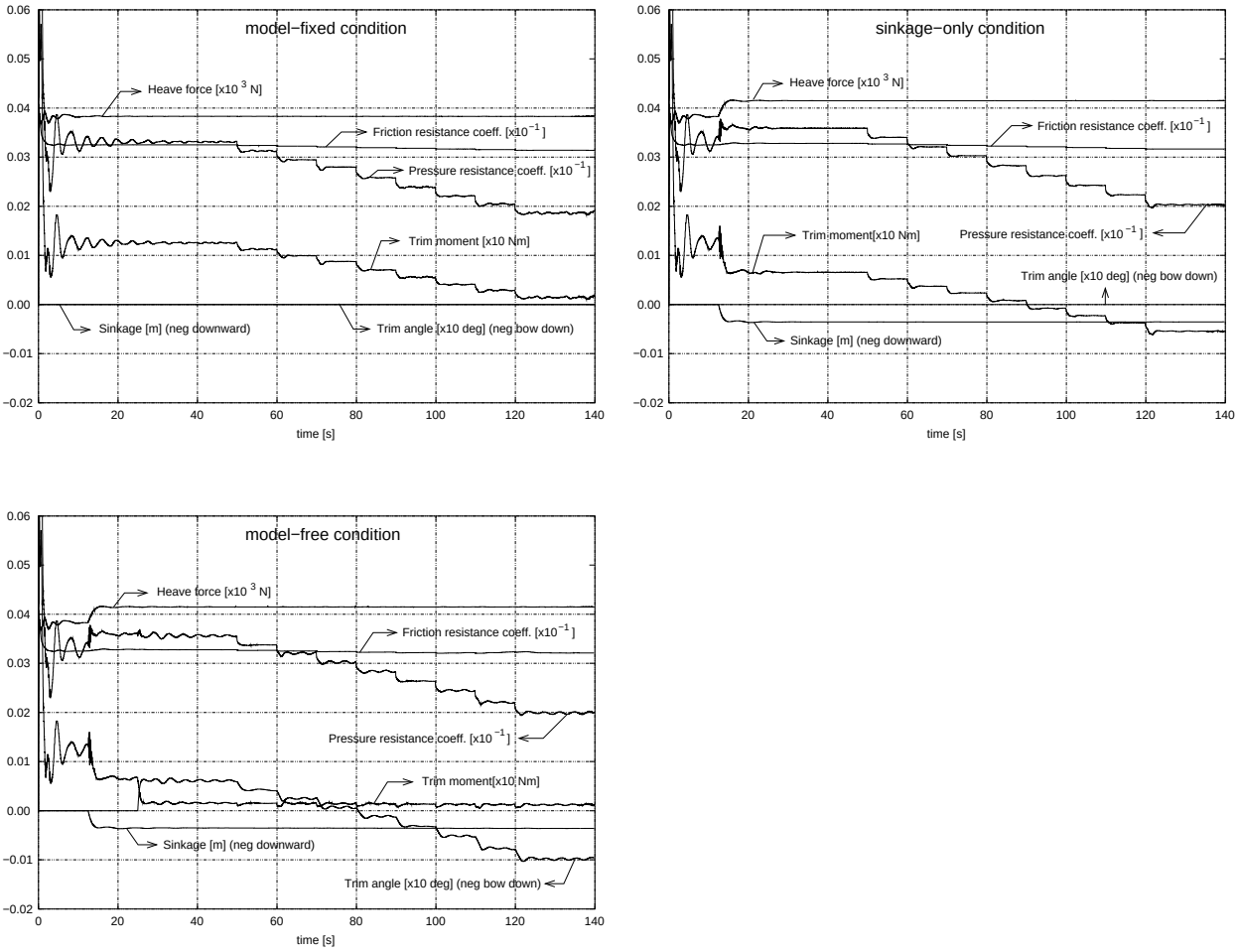

Fig.2: Convergence history the for 0°-drift calculations in the model-fixed (top left), sinkage-only (top right) and model-free (bottom) conditions

3.2 Blunt-bow ship model (Breaking waves)

Computational studies of the wave breaking ahead of the bow of a very full hulls are difficult and rare. The Ship Research Institute (SRI) in Tokyo measured bow-wave breaking in front of a blunt-bow ship model, Fig.3. The computations presented here are an effort to numerically simulate the flow under the same conditions as in the experiments at SRI. In a first step, computations in the model-fixed condition were performed and the bow-wave breaking pattern was compared with the experimental data available, *Azcueta et al. (1999a)*. In a second step, the model-free condition was investigated (sinkage and trim), and the results were compared with those of the model-fixed condition. After performing the computations in model-free condition, the model tests were repeated at SRI for the sinkage-only condition.

In the waterplane, the bow of the model is a semi-circle with radius $R = 0.3$ m. It is followed by a parallel middle body of 1 m length, and a stern of 0.7 m length, prescribed as a spline. The total length of the model is 2.0 m and the beam 0.6 m. The same shape of the waterplane extends 0.2 m above the design waterline up to the deck and 0.3 m beneath the design waterline. There, half a

body of revolution, obtained by rotating the waterplane around its longitudinal axis, is attached to complete a total draft of 0.6 m. The model speed was set at $v_o = 1.697$ m/s. The Reynolds number based on the hull length was $3.4 \cdot 10^6$. Three grids (103,950 CVs, 411,180 CVs, 2,147,628 CVs) were used in order to assess the grid dependence of the computed wave patterns. Fig.4 shows the coarsest grid (matching block-structured). The medium grid was obtained by refining the CVs in all directions in a region extending horizontally over the whole computational domain and vertically 0.16 m above and below the design waterline. The size of this region was established using the free-surface elevation previously obtained on the coarse grid as a reference. The finest grid was obtained by refining the medium grid in a region restricted horizontally to about half a model length around the model.

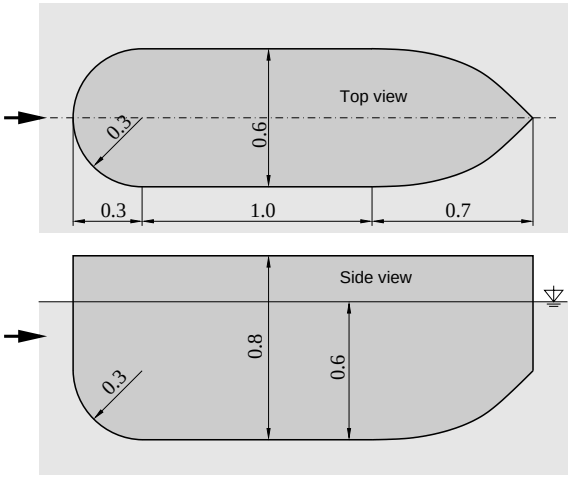

Fig.3: Sketch of the used model

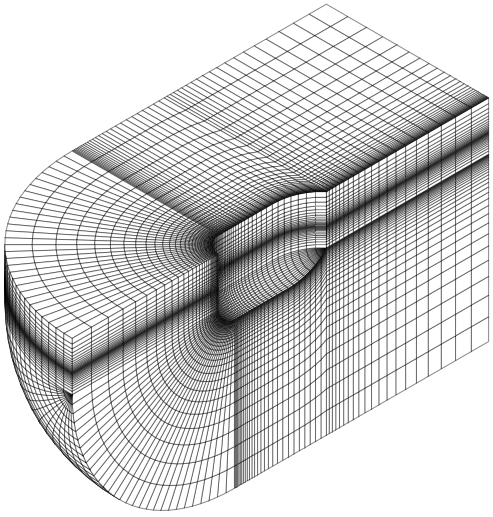

Fig.4: Coarse grid used for the simulations

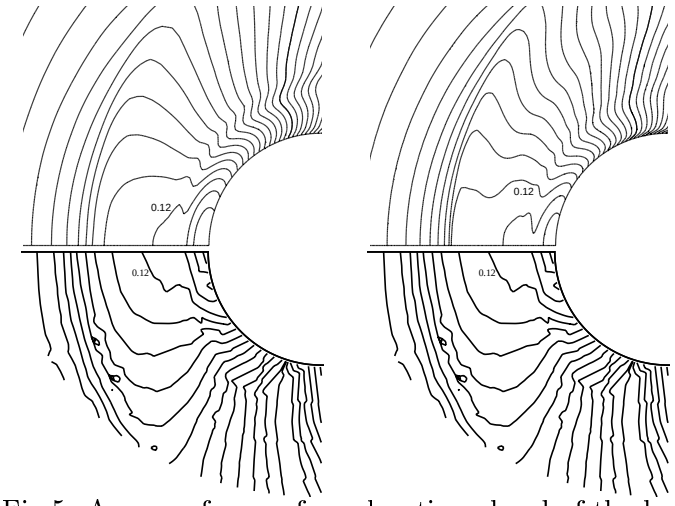

Fig.5: Average free-surface elevation ahead of the bow: measurement (below; courtesy of SRI) and computation (top left: medium grid; top right: fine grid). Interval between contours 0.01 m

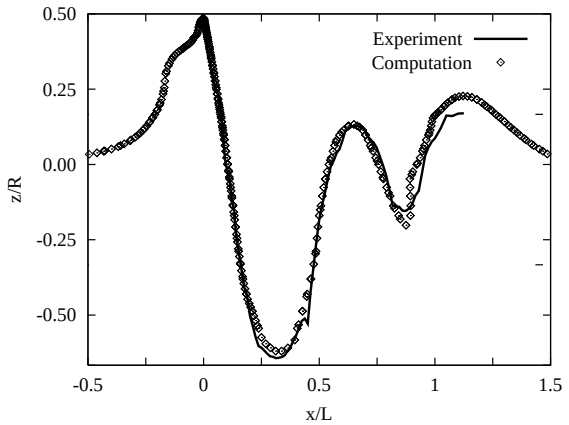

Fig.6: Measured and computed wave elevation along the hull, (CFD on medium grid, model-fixed condition, exp. by SRI)

The model-fixed simulations were carried out until a periodic oscillation of pressure drag was obtained over many periods. This was typically the case after about 4000, 6000, and 8000 time steps for the coarse, medium and fine grid, respectively. This number of time steps corresponded to a simulation time of 40 s or the time taken for a water particle to travel $20L$. Δt was chosen so that a Courant number of 1 was not exceeded. First, only one outer iteration per time step was used until

the periodic flow was reached, and then 20 iterations were set over a few oscillation periods to obtain a good average of forces. A constant blending of 90% CDS was used for all cases. While the friction drag remains nearly constant during the simulation, the pressure drag oscillates typically by about $\pm 5\%$ around the mean values (shown in Table IV). The oscillation period for the pressure drag for all grids is about 2.5 s, equal in this case to the time required for a water particle to travel $2L$. However, the period of the breaking bow-wave is much smaller at approximately 0.6 s. The oscillations in C_P are influenced much more by the much larger breaking wave at the side of the model, which initiates a back and forth movement of the stern wave. Fig.5 shows the time-averaged (over the last 10 s or about 16 periods of wave breaking) free-surface elevation in the bow-wave region computed on the medium and fine grid with experimental data from SRI. A very good agreement is observed between experiment and simulation on the medium grid, while the finest grid shows a shorter distance from the bow to the breaking wave crest. One cause for the fact that the results obtained on the finest-grid do not agree with experimental data as well as those on the medium grid could be that the small-scale free-surface disturbances introduce additional diffusion effects on the breaking wave which are not modeled in the simulation. It may be that the amount of numerical diffusion on the medium grid is just of the right order to model the above named effects. With a finer grid but without resolving the small-scale turbulent fluctuations of the free surface, the wave becomes too sharp and hence also shorter. Fig.6 shows computed and measured wave elevations along the hull (medium grid). The bow is located at $x/L = 0$ and the tip of the stern at $x/L = 1$. The agreement is satisfactory.

In addition to the computations in the model-fixed condition, computations with the model free to sink and to trim were performed. In this case, the trim angle is significantly large due to the high Froude number, changing the whole wave breaking pattern. The lateral and upper boundary, formerly a slip-wall condition, were changed to inlet condition. Also the position of the center of gravity and of the towing force, as well as the moments of inertia of the model (not known from the experimental specifications) had to be estimated. The delays factor DF and the moments of inertia were varied and a consistent set of values to attain good convergence was used, Fig.7.

The UDS-CDS mixing ratio was in this case kept constant at 90% CDS. Initially, the flow around the fixed model was computed until a periodic flow had been established by 30 s simulation time. After 30 s, the constraint for the vertical translation, i.e. the sinkage, was released. At this stage, the sinkage converges to a value of about -50 mm. The vertical velocity, which is maximal shortly after being released, converges to zero. Meanwhile, the vertical force becomes larger, reaching the displacement of the model (2620 N for one half of the model). After 60 s the constraint for the rotation around the transversal axis, i.e. the trim, was released. The trim angle grows larger until it converges at $-3.6°$, trim by the bow. The trim moment, which was constant at about 40 Nm before 60 s, converges to zero thereafter. The same happens with the trim angular velocity which is maximal at the time of releasing the motion and decreases to zero thereafter. While the model is going down by the nose, the sinkage adjusts from 50 mm to about 12 mm at steady-state.

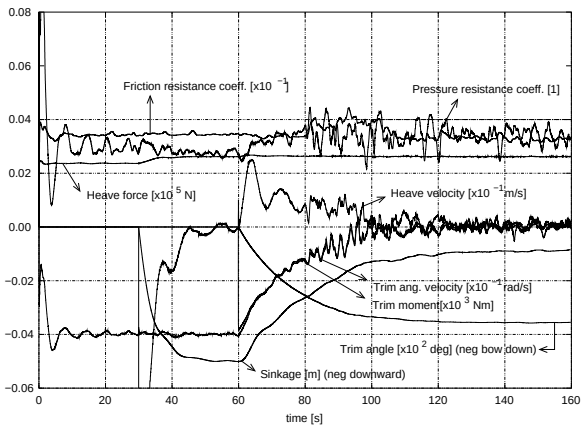

Fig.7: Time convergence history of forces, velocities and motions on medium grid

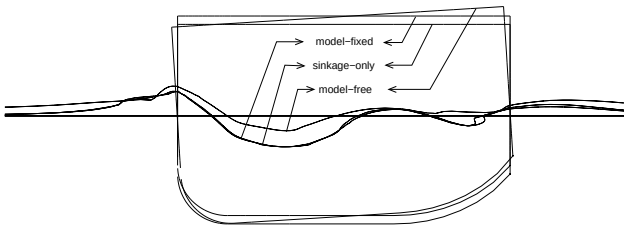

Fig.8: Model position and wave profile for the model-fixed, sinkage-only and model-free conditions

Fig.8 shows the average position of the model and the contour of the free surface for the three time instants; 30 s (no sinkage and no trim), 60 s (sinkage only) and 160 s (sinkage plus trim). While the wave profile does not change much for the sinkage-only condition, it looks quite different for the final trimmed attitude. The water level ahead of the bow rises sooner, the bow-wave amplitude becomes larger, the shoulder wave trough is substantially shallower, and the stern wave hardly breaks, but becomes higher in the wake. The wave patterns around the bow as computed on the medium grid for the model-fixed and model-free conditions shows the large differences between the two conditions, Fig.9.

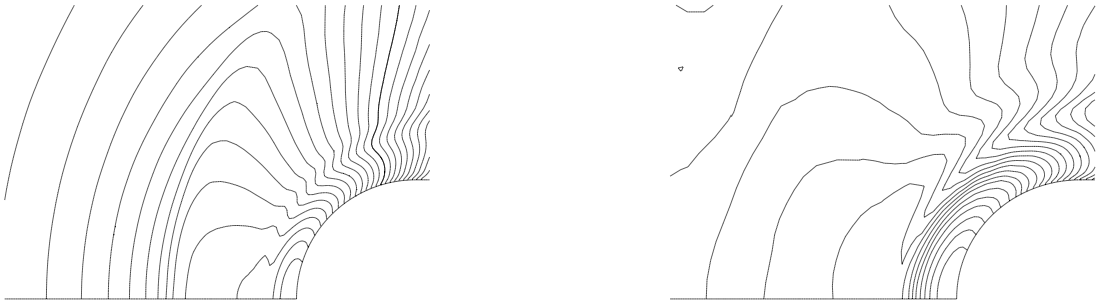

Fig.9: Wave heights ahead of the bow for the model-fixed (left) and model-free (right) conditions (medium grid)

The difference in free-surface shape is associated with large changes in force coefficients. Table IV lists for the coarse and medium grids the computed friction, pressure and total resistance coefficients, as well as wetted surface, sinkage and trim, for the model-fixed and model-free conditions. Unfortunately, no experimental values (resistance, sinkage and trim) are available for these two conditions. The values in this table are for a constant blending of 90% CDS. The size of the time steps were $\Delta t = 0.01$ s and $\Delta t = 0.005$ s (constant) for the coarse and medium grids, respectively. To obtain a good average of forces, 20 outer iterations per time step were set over a few periods (also for the animations). The wetted surface underway increases by about 9%, the total resistance coefficient by 17% and 26% for the coarse and medium grid, respectively, mostly due to the predominant C_P values. Sinkage and trim are predicted slightly smaller on the medium grid than on the coarse one. The CPU time per time step was again about 50% larger for the model-free than for the model-fixed condition.

After performing the computations in model-free condition, the model tests were repeated at SRI for the sinkage-only condition, and resistance and sinkage were measured. The results of the computation for the sinkage-only condition (not shown in Table IV) are extracted from the time history of forces and motions, Fig.7, averaging the values between 55 s and 60 s. The computed resistance (140 N) on the medium grid differs from the measured resistance (132 N) by only 6%. The computed sinkage (0.050 m) differs from the measured one (0.046 m) by 8.7%. The agreement in resistance and sinkage is thus satisfactory. Unfortunately, the computed trim could not be validated so far. However, the series of towing tank tests will be extended for the model-free condition as well, so that this test case could become an interesting benchmark in the future.

Table IV: Resistance coefficients, trim and sinkage for the blunt-bow ship model

grid	cond.	C_P	C_F	C_T	wetted surf.	sinkage	trim
coarse	fixed (fx)	0.0303	0.0321	0.0335	1.46 m^2	0.0 mm	0.00°
	free (fr)	0.0358	0.0346	0.0392	1.58 m^2	−11.3 mm	−3.61°
	(fr-fx)/fx	18.1%	7.8%	17.0%	8.2%		
medium	fixed (fx)	0.0294	0.0342	0.0328	1.46 m^2	0.0 mm	0.00°
	free (fr)	0.0378	0.0358	0.0414	1.60 m^2	−8.8 mm	−3.55°
	(fr-fx)/fx	28.6%	4.7%	26.2%	9.5%		

4 Freely floating bodies

4.1 Drop tests (Plane motion)

A test case for which experimental data exist was chosen to validate the applicability of the implemented computational method for the time-accurate simulation of plane motions with 3-DOF. Symmetric and asymmetric drop tests with a prismatic hull have been experimentally investigated by *Peterson et al. (1997)* and theoretically by *Xu et al. (1999)*. The motivation of such investigations resides in the need to understand the dynamic response of vessels such as planing boats operating at high speed in a seaway during asymmetric water impacts. Other interesting aspects in this context are the avoidance of hull damage caused by bow flare slamming and the evaluation of shock reduction concepts for military craft.

For an accurate simulation of water-entry phenomena and the associated ship responses and slamming forces, strong deformation of the free surface including jets, sprays, splashing, air trapping, breaking waves and cavitation have to be considered. Computations by *Muzaferija (1998)* showed that this method is well capable of considering all these flow features with the exception of cavitation. Furthermore, a fairly good agreement of predicted forces and pressure distributions with experimental data was obtained. However, in these computations, the body motion was prescribed using the time history of the motion from the model tests and only symmetric water impacts were investigated. Most other calculations of water-entry phenomena until now have also been of a deterministic type, i.e. the body undergoes a forced motion prescribed as measured or previously calculated by other means, *Schumann (1998)*, *Sames et al. (1998)*. *Sames et al. (1998)* stress the need for a careful determination of the entry velocity histories to obtain realistic design slamming pressures, i.e. an estimation of the entry velocity is not good enough. Coupling the flow solver with a rigid-body motion solver is the best way to achieve this. In the present simulations the body trajectory, velocity and forces (in 3-DOF) are obtained from the flow forces acting on the body, starting from the initial condition, without the need for prescribing the body motion. Unlike the experimental drop tests, the simulations do not only yield the vertical and angular accelerations, but also the transverse acceleration, as well as the water impact forces at each point of the model as a function of time.

The physical model used by *Peterson et al. (1997)* was a high aspect ratio (0.61 m · 2.44 m) prismatic wedge with 20° deadrise. It was dropped from different heights, with different weights, and with initial zero or non-zero heel angles. It was instrumented with accelerometers for recording the roll and vertical acceleration time history. Following test conditions were numerically simulated:

- Symmetrical drop, light-weight condition ($W = 122$ kg)
- Asymmetrical drop (5° heel), light-weight ($W = 124$ kg, $I_{xx} = 8.85$ kgm^2)
- Asymmetrical drop (5° heel), medium-weight ($W = 293$ kg, $I_{xx} = 10.95$ kgm^2)

The drop height was 0.61 m, measured from the water to the keel of the wedge. The position of the center of gravity was at the symmetry plane and 0.216 m above the keel for the light weight and 0.165 m for medium weight. In the numerical model, the configuration was reduced to two dimensions. Thus, weight and moments of inertia had to be reduced to the model slice of 0.05 m. In the integration of the body motion equations, no delay in the body velocity was applied (see Eq.(16)), since in this case a time-accurate simulation of an unsteady process was sought. The same numerical mesh was used in all cases, Fig.10. It was relatively coarse with less than 15,000 CVs, and extended 2 m to the sides, 1 m from the keel upwards, and 1.5 m from the keel downwards, i.e. with 0.9 m being filled with water at the initial condition. Since no side current is present in this configuration, no inlet and/or outlet boundary conditions have to be specified. Instead, the hydrostatic pressure (and the volume fraction) is specified at all flow boundaries (side, top and bottom), since it is assumed that the pressure disturbances are minimal that far away.

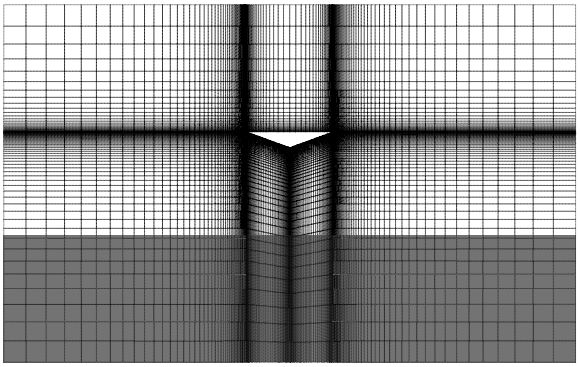

Fig.10: Mesh for drop tests with wedge. Shaded zone indicates water at rest

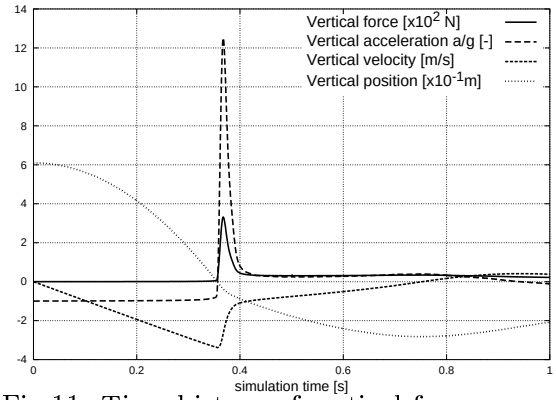

Fig.11: Time history of vertical force, acceleration, velocity and position for symmetric drop test simulation

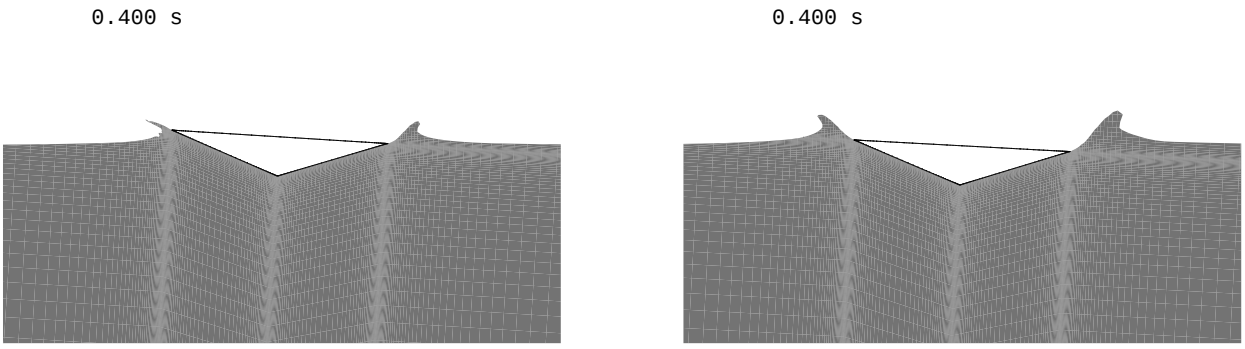

Fig.12: Time instant $t = 0.4$ s for the asymmetric drop in light-weight (left) and medium-weight (right) conditions

Fig.11 shows what the dynamic response of such a drop test generally looks like. At time $t_o = 0$, the vertical position is +0.61 m, force and velocity are zero and the vertical acceleration, which has been normalized with the acceleration of gravity $g = 9.81$ m/s, equals -1 (vertical axis points upwards). It takes only 0.35 s for the wedge to reach the water, where the vertical velocity is at its maximum. Vertical force and acceleration (in the asymmetrical drops also transverse and rotation) then peak for a short interval of 0.05 s. After that, position, velocity and acceleration oscillate around zero as the wedge slowly heaves and reaches its equilibrium position. The remaining vertical force equals the weight of the slice of the model (approx. 24.5 N). In the following, we will concentrate only on the short interval between 0.35 and 0.45 s, when the large forces and responses take place. Fig.12 shows snapshots at the instant $t = 0.4$ s as the wedge penetrates the water for the asymmetric drops.

Fig.13 compares the simulated vertical and angular acceleration, vertical or impact velocity and angle of heel for the asymmetric drop tests with experimental data of *Peterson et al. (1997)*. The mean vertical acceleration from the experiment is the average of the two accelerometers, one on the starboard and one on the port side of the model. The experimental results contain mechanical vibrations associated with structural resonance, making a precise quantitative comparison between simulation and experiment difficult. Nevertheless, the comparison shows good agreement both for the magnitude and timing of the maximum accelerations and velocities, and for the time history of the remaining dynamic response. The major differences seems to be a phase lag of 0.002 s and an over-prediction of the magnitude in the vertical acceleration. The phase shift can be caused by a time discretization error at the start of the simulation. It is relatively small though, less than 0.6%, if the whole falling time before the wedge reaches the water is considered. The over-prediction in magnitude may be due to the neglect of three-dimensional effects, as found by *Troesch and Kang*

(1990), Zhao et al. (1997).

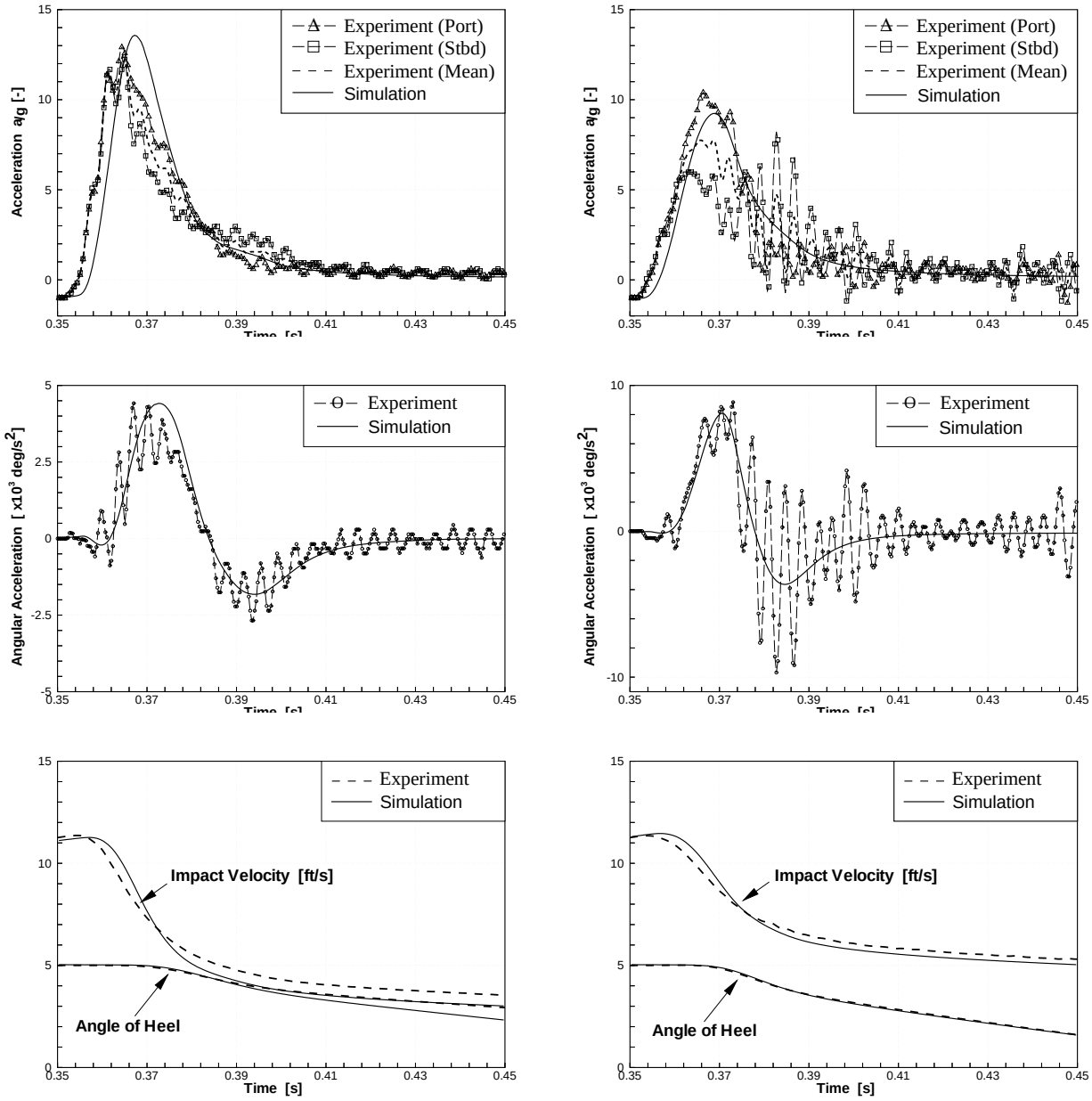

Fig.13: Measured, *Xu et al. (1999*, and simulated results for the asymmetric light-weight (left) and medium-weight (right) conditions

This test case was also used to assess the effect of Δt and the number of outer iterations per time step on the response dynamics. Fig.14 shows how the vertical and angular accelerations vary for three different (constant) Δt. It corresponds to the simulation in the asymmetric light-weight condition with 5 outer iterations per time step. With a Δt four times as large, the amplitudes of the acceleration curves diminish by more that 25%. Also the position of the peak shifts a little. The figure only shows vertical and angular acceleration responses, but the same applies for forces, velocities and motion. Results converge monotonically with decreasing Δt. The correct choice of Δt is very important to obtain the dynamic response. Fig.15 shows the effect of reducing the number of outer iterations per time step from 20 to 5 for $\Delta t = 0.0005$ s. The effect is small compared to the effect of changing Δt, but it becomes larger if Δt is larger. This point is summarized in Table V, which lists the CPU time needed to simulate 0.5 s on a Pentium III 450 MHz for each case. Labeled as "2^{nd} best" is a calculation that represent the best compromise between accuracy and computation effort.

Table V: CPU time on Pentium III 450 MHz (asymmetric drop; light-weight condition)

outer iter./time step	Δt	total outer iter.	CPU time	remarks
20	0.0005 s	20000	7.0 h	best
20	0.0010 s	10000	3.5 h	
5	0.0005 s	5000	2.0 h	2^{nd} best
5	0.0010 s	2500	1.0 h	
5	0.0020 s	1250	0.5 h	

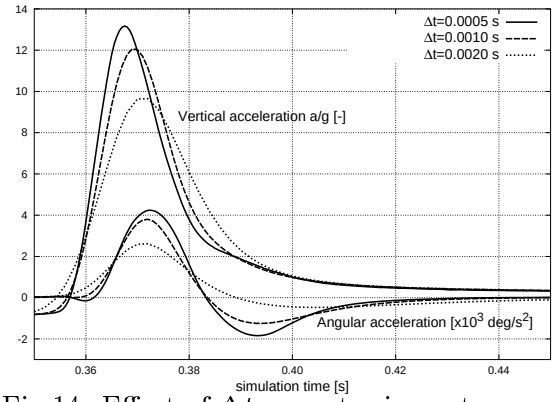

Fig.14: Effect of Δt on water impact dynamics (5 iter./time step)

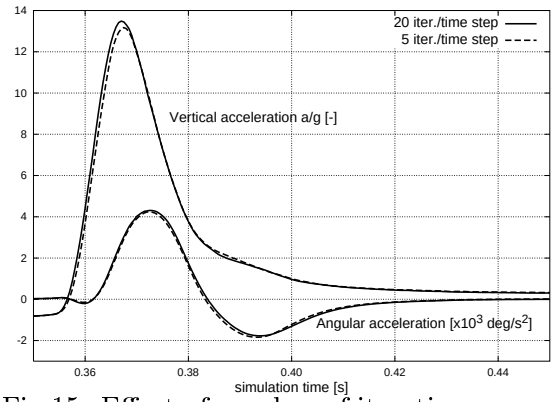

Fig.15: Effect of number of iterations per time step on water impact dynamics for $\Delta t = 0.0005$ s

All test calculations performed in this work so far had a constant Δt. However, other alternatives should be kept in mind. E.g., in this drop test, using a large Δt in the constant acceleration phase from t_0 up to 0.35 s and then a smaller one when the wedge impacts the water would have produced better results at lower computational cost. It still would be a better alternative to use a time-marching method with a step-size control which dynamically changes Δt, so that the time resolution improves in those phases when the body (or fluid) acceleration changes most.

4.2 Boat section (Plane motion)

The next application case shows a boat main section undergoing a large amplitude roll motion coupled with heave and sway (2-D planar motion). In order to characterize the roll behavior of a ship, it is essential to estimate the roll damping already at the preliminary design stage. The estimation procedure has so far relied heavily on experimental data, in the form of traditional tank testing with the prototype or in the form of correlations of historical experimental data. Of the many quantities that characterize roll motion, the non-linear damping parameter is the most crucial one for ship response. It is very difficult to estimate because the mechanisms that govern roll damping are very complicated. The individual mechanisms that lead to roll damping are: the creation of waves when the ship rolls, the damping due to viscous effects in real fluids, such as skin friction, viscous separation and formation of eddies near sharp edges, as well as the normal pressure force on the keels and the lifting forces on the hull sides when the ship is rolling underway. All these components are a function of forward speed. For small forward speeds, so called roll extinction tests can be used to determine the roll damping. In these tests, the model is inclined to a relatively large roll angle and then suddenly released. The model then oscillates at its natural frequency. The information in the time history of the motion is then used to determine the roll damping coefficient at the roll natural frequency of the model.

I simulated such a roll extinction test using the midship section of a sailing boat as a test case. Two configurations were investigated – the bare hull and the hull with a fin keel – and the effect of the keel on the damping coefficient was examined. Similar 2-D, no-forward-speed roll simulations can be of use to investigate the low-frequency oscillation of moored floating bodies. The calculated damping coefficients can also be used to feed a strip-theory method when the effect of forward speed

is negligible. Two-dimensional tank testing is hard to carry out because large aspect ratio models are necessary to create a two-dimensional flow. Therefore, no appropriate test cases were found in the literature for comparison. At a second stage, this test was extended to three dimensions and forward speed for the bare hull configuration.

The geometry of the boat corresponds to a modern sailing yacht of 10 m length and 3 m beam, built in Germany by Dehler. The same boat class was extensively used to investigate sailing forces under real conditions by means of a full-scale sailing dynamometer by *Brandt et al. (1997)*. The numerical mesh for the 2-D simulation is relatively coarse. It has 64 and 32 CVs in sectional girth and radial directions, respectively, Fig.16. It was extended with a block above deck to allow large roll angles. The total number of CVs is 5192. The spacial resolution around the keel is not sufficient to accurately capture the eddies which appear in that region, but further local refinement could be used, if this were the goal of the investigation. The computational domain is a cylinder of 20 m radius, i.e. more than six times the beam of the boat. The size of the time step chosen is $\Delta t = 0.0025$ s. 20 outer iterations per time step were performed. The mass of the model was reduced to the section slice, so that the boat floats at its design waterline. The vertical position of the center of gravity was estimated to be at the height of the design waterline, which is a common value for a sailing boat. The roll radius of gyration was estimated to be $k_{x_G} \approx 0.33B$. No delay was applied to the body velocity (Eq. (16)) in the integration of the body motion equations. The same type of pressure boundary condition as for the drop test simulations was used for the flow boundaries, i.e. for the outer cylinder and the top lid.

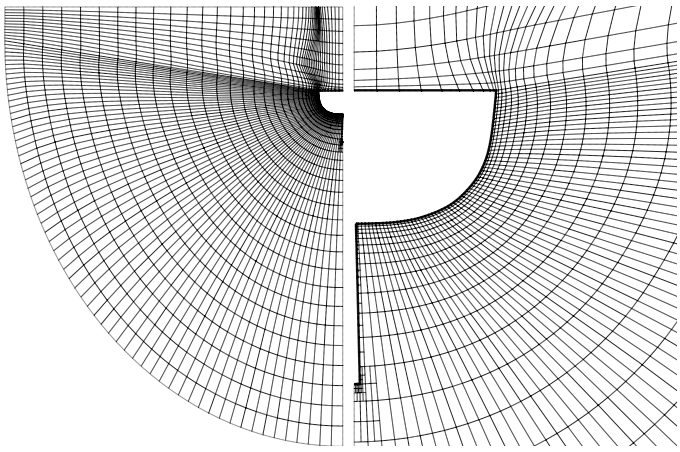

Fig.16: Mesh used in the simulations for the rolling boat section

To induce a roll motion, the boat section was initially inclined 30° in calm water to one side, and then abruptly released to roll freely, Fig.17. Because the mesh is so coarse in the block above the deck, the free-surface contour smears when the boat rolls and that portion of the mesh dips into the water. But when the free surface traverses again through a region of better resolution, it automatically becomes sharper. At 1.1 s the boat is in the upright position, for which this mesh is optimal. The numerical mesh was deliberately generated so coarse in order to demonstrate this fact. Another good characteristic of the computational approach is that the floating body is actually allowed to roll over such a large angle that the top of the computational domain dips into the water, without causing numerical difficulties. This point will not be demonstrated here, but has been observed in many simulations. The robustness of the method in this point gives flexibility to perform different situations with the same mesh. Substantially, this means that the mesh must not necessarily be restricted to a pre-determined roll angle range, but can be good for a range of angles, and still acceptable for larger ones.

Fig.18 shows the time history of sway, heave and roll motion for the simulations with and without the keel for the first one and one and a half roll periods, respectively. The center of gravity and the roll moment of inertia were set equal for both cases – with and without the keel – to assess the viscous,

non-linear damping due to the presence of a large surface across the flow.

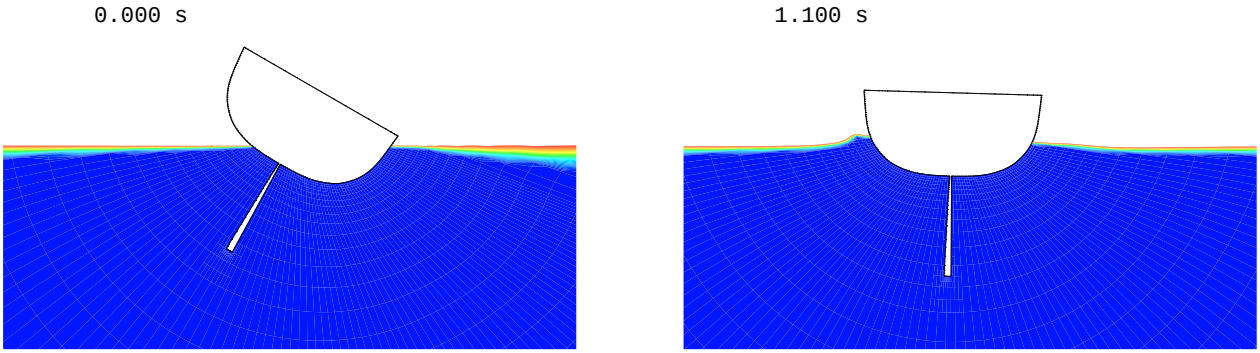

Fig.17: Snapshots in the roll simulation: initial state (left) and instant 1.1 s thereafter (right)

The section without the keel completes the first period in 2.9 s and the roll angle decreases by 6.4° in this period of time, while the section with the keel needs 4.3 s to reduce the roll angle by 18.8°, Table VI. However, from that point onwards, the section without the keel oscillates at a more or less constant roll amplitude. This is because the waves generated by the body reflect at the non-physical flow boundary at the side, and a sort of roll resonance takes place.

Table VI: Maxima and minima of the roll motion and their timing with corresponding logarithmic decrement and roll period

	2-D no keel				2-D keel			
j	φ_j [°]	t_j [s]	δ	T_φ [s]	φ_j [°]	t_j [s]	δ	T_φ [s]
0	−30.00	0.000			−30.00	0.000		
0.5	+26.46	1.427	0.193	2.87	+18.08	2.155	1.003	4.24
1	−23.56	2.860			−11.18	4.325		
1.5	+22.96	4.305	0.013	2.97	+6.45	6.310	1.093	3.58
2	−22.85	5.792			−3.56	8.100		
2.5	+23.08	7.307			+2.35	9.692		

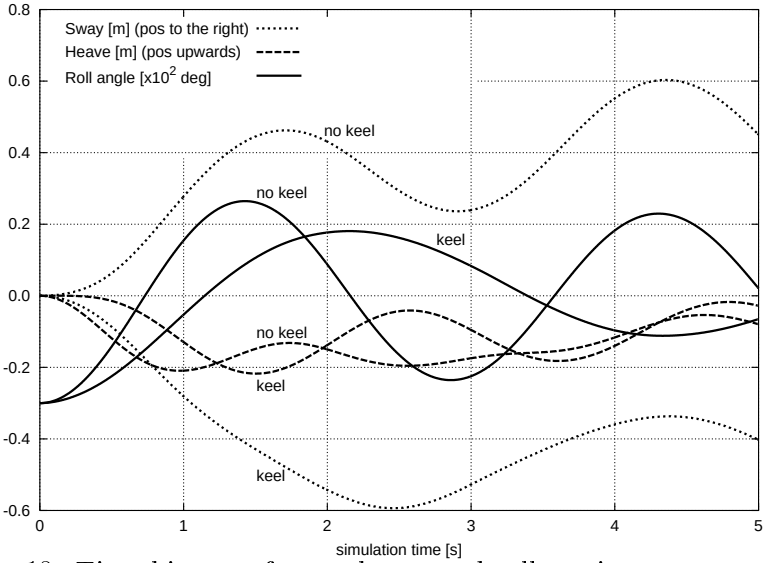

Fig.18: Time history of sway, heave and roll motion for roll simulations with and without keel

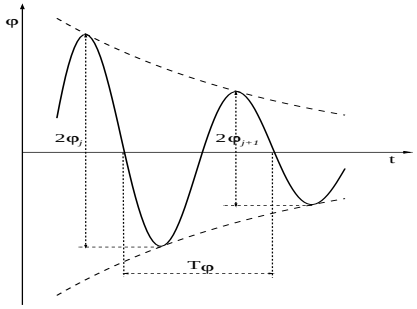

Fig.19: Logarithmic decrement and roll period

Table VI lists maxima and minima of the roll motion φ_j and their timing t_j with the resulting roll periods T_φ and logarithmic decrements δ. The logarithmic decrement together with the roll period characterizes the roll damping coefficient, Fig19:

$$\delta = -\ln(\varphi_{j+1}/\varphi_j) \tag{23}$$

$$T_\varphi = (t_{j+1} + t_{j+1+1/2})/2 - (t_j + t_{j+1/2})/2 \quad \text{for} \quad j = 0, 1, 2.... \tag{24}$$

The logarithmic decrement as well as the roll period for the case with the keel are much larger than those without the keel. Another big difference induced by the keel is in the sway response. As the hull section rights up, the keel acts like a lever pushing the hull to the left side, in the coordinates of Fig.17 (dotted line in the negative area in Fig.18). Without the keel the hull presses the water to the left, and gets an impulse to the right (dotted line in the positive area).

4.3 Sailing boat in planing condition (3-D case)

The next example is the simulation of the motions of a sailing boat in 4 DOF. Such a boat was chosen as test case, since it undergoes large heel angles or rolling motions, as well as large trim angles due to the high speeds at which it sails. High-speed planing hulls are interesting from the point of view of their dynamic stability, specially when slamming and rolling in a seaway. Furthermore, in the steady-state planing condition, there is an optimum in transom size and shape, depending on speed and trim. For power boats, the resistance can be optimized with the proper choice of the planing wedges or stern flaps. The simulation introduced here represents the further step towards tackling such complicated questions by means of viscous flow computations.

In the present simulations, the boat undergoes a coupled roll, pitch, sway and heave motion at full constant speed in calm water. Initially, it is constrained in an inclined position until the steady-state flow is reached. Then, the motion constraints for the four DOF are released simultaneously initiating in this way the free motion. The surge and yaw motions were kept constrained. The boat speed chosen was relatively high ($v_o = 7$ m/s; $F_n = 0.7$), to ensure that it is planing in the free condition. The initial heel angle of 15° (to starboard) ensures large roll motions in the transient condition. This initial (steady-state) sailing position is not realistic, since it is too fast for a boat sailing close-hauled. However, the final planing attitude at that speed is very well possible for these kind of light boats under sail power sailing downwind. To simplify the 3-D simulations, only the bare hull was taken into account, i.e. without keel and rudder. The numerical mesh was conceived to allow large rolling motions of up to 30° without the top boundary dipping into the water. It is similar to the 2-D mesh but with only 32 CVs in sectional girth direction, without the additional block above the deck and with a slightly finer resolution at the hull wall to resolve the boundary layer. It has a total of 280,000 CVs. The longitudinal position of the center of gravity was calculated for the boat in the upright condition floating on an even keel. The vertical position was the same as in the 2-D case. The pitch radius of gyration was estimated to be $k_{y_G} \approx 0.15L$, and the roll radius of gyration was the same as in the 2-D case ($k_{x_G} \approx 0.33B$). The products of inertia were set equal to zero. The boundary conditions were the same as for the model-free computation with the Series 60 and blunt-bow models; the front, side, bottom and top flow-boundaries were specified as an inlet of constant known velocity and known volume fraction distribution, and the wake flow-boundary as a zero-gradient boundary of known pressure distribution (hydrostatic pressure). Since the Reynolds number of the flow is not too high ($R_n = 7 \cdot 10^7$), these simulations are performed for the full scale boat using the standard k-ϵ turbulence model with wall functions.

Since this test case undergoes a transient phase of large amplitude motions and also reaches a steady-state final position, it is well suited to analyze the two types of problems, the steady and the unsteady ones. The main difference between the simulation of freely-floating body motions and the calculation of the steady free-surface problems is that in the steady case the transient characteristic of the motion is not relevant, but rather a fast convergence towards the final state is desired. Thus, different computational efforts are required in both cases. To achieve fast convergence towards the steady-state solution, one can use a large Δt, as well as perform as few iterations per time step as possible. In this case, it is necessary to retard the body velocity to avoid numerical difficulties using the delay factor DF of Eq.(16). In the present study, many combinations of Δt, DF and iterations per time step were investigated and the CPU time taken for convergence was checked, Table VII. In the first 5 cases listed in Table VII, only the determination of the steady-state planing attitude of the boat was intended. Fig.20 shows the time history of motions for case #1. In the last three

cases listed in Table VII the unsteady motion was the focus of attention (see Fig.21 for case #8). All computations were started with the full boat speed in the inclined position and run over 2,000 time steps (50 s simulation time) until the steady-state solution for that condition was reached. At 50 s, the four DOF were simultaneously released. Depending on the used parameters, the time histories of motion showed in some cases overshooting and oscillations before settling down to a constant value, while in other cases convergence was not achieved at all (see remarks in Table VII).

DF strongly influences the convergence behavior of the motions. The less the body velocity was delayed for a given Δt and number of iterations, the stronger the oscillations, until the motion finally diverged. This is shown in Table VII, where case #1 with $DF = 0.5$ converged, case #2 with $DF = 0.7$ oscillated and case #3 with $DF = 0.9$ diverged. In cases #4 and #5, 5 iterations per time step were used and convergence towards the steady-state planing attitude was again achieved. The pitch angle converged at about 5° nose up and the heel angle converged towards a value slightly above 0°, maybe due to small asymmetries in the flow. Because for the sway motion no restoring force applies (indifferent equilibrium), the boat keeps moving sidewards. This may be the reason for the asymmetry of the flow which induces the small roll angle. The sway motion depends on the initial impulse when the boat rights up, and this in turn on the delay factor applied to the body velocity. Thus, the sway motion looks different for each case. In all these first five cases, Δt was the same as the one used for the model-fixed computation, i.e. in the first 50 s simulation time. That means, these slow adjustments in running attitude do not require more time accuracy than is needed for computing the model-fixed condition, but undoubtedly more time steps have to be performed to reach the converged planing attitude.

To obtain a time-accurate simulation of the motion, the body velocity should not be delayed. Furthermore, a better convergence in each time step is required. Consequently, the number of outer iterations in the last three simulations was kept at a minimum of 5. The dynamics of the simulated motion are very sensitive to Δt. With the same Δt like the one used in the calculations before (#1 to #5), no motion convergence is obtained so that the boat capsizes. When Δt is halved, an undamped rolling oscillation over many periods with an amplitude larger than the initial one is obtained. With a still smaller Δt, the motion dynamics looks realistic, i.e. a damped rolling motion was simulated, see case #8, Fig.21. However, due to the lack of experiments, this could not be validated. Without the keel and rudder, the roll motion is slightly damped, and it takes many cycles to die away completely. The pitch angle converges to exactly 5°, i.e. a bit smaller than for the steady-state calculation. This difference might be due to the improved accuracy obtained with a smaller Δt. The pitch motion is quite fast, i.e. the boat reaches the final position with the nose 5° up in about 2 s or one roll period. The vertical position of the center of gravity (heave) depends on the heel angle, and it also displays a coupling with the other motions. After 15 s it is still moving down as the wave pattern grows larger. If the simulation were still continued for many seconds, then the heave might converge to a value close to those of the previous cases.

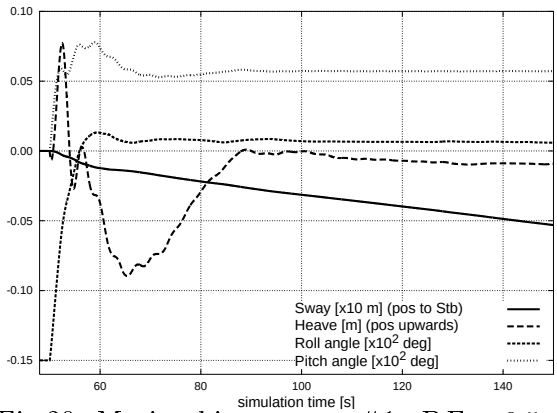

Fig.20: Motion history case #1: $DF = 0.5$; 1 iter./time step; $\Delta t = 0.025$ s

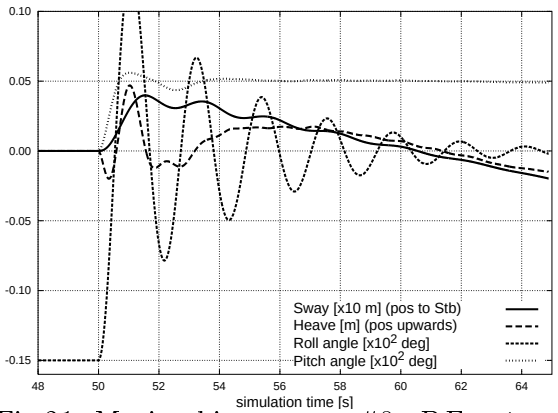

Fig.21: Motion history case #8: $DF = 1$; 5 iter./time step; $\Delta t = 0.005$ s

Table VII: Parameters of the numerical method varied for convergence towards steady-state floating position (#1 to #5) and free motion (#6 to #8). CPU time on Pentium III 450 MHz

case	DF	iter. / time step	Δt	convergence			Remarks
				sim. time	CPU	iter.	
#1	0.5	1	0.0250 s	100 s	30 h	4,000	steady-state flow
#2	0.7	1	0.0250 s	-	-	-	strong oscillations
#3	0.9	1	0.0250 s	-	-	-	motion divergence
#4	0.7	5	0.0250 s	40 s	60 h	8,000	steady-state flow
#5	0.9	5	0.0250 s	40 s	60 h	8,000	steady-state flow
#6	1.0	5	0.0250 s	-	-	-	no convergence
#7	1.0	5	0.0125 s	-	-	-	undamped rolling
#8	1.0	5	0.0050 s	15 s	112 h	15,000	realistic motion

5 Conclusions and further work

The numerical resistance prediction is improved by taking into account the changes in trim and sinkage. The proposed numerical approach is capable of predicting both small and large changes in trim and sinkage. For the Series 60 case, the model-free calculation predicts the total resistance 10% larger than the model-fixed calculation, thus improving the agreement with the measured value from about 14% to about 6% under-prediction. The comparison of measured and computed sinkage, trim and heel angles for the Series 60 hull is satisfactory. The need for accurate documentation of the experimental set-up for validation is thus obvious. The results for the straight-ahead condition agreed better with measurements than those for the drift condition, since the asymmetric flow is more complicated than the symmetric one. In the case of the blunt-bow ship model, the total resistance on the medium grid increases by 26% due to the squat, and the large changes in running attitude produce large changes in the wave pattern and the wave-breaking dynamics. For the sinkage-only condition, the computed resistance and sinkage over-predict the measured values by 6% and 9%, respectively.

The moments of inertia influence the transient response, but not the steady-state solution. They can thus be varied in order to obtain a fast convergence. The same is valid for the delay factor used to retard the body velocity. Both the delay factor and the moments of inertia have a similar effect on convergence, and should be chosen consistently. The increase in CPU-time for computing the model-free condition is about 50%. This is due to the transformation – translation and rotation – of the whole grid geometry into the new position after each time step, which is computationally very expensive, as well as to some extent due to the calculation of the forces and moments, integration of the equations of motion, more complicated boundary conditions, etc.

The single-grid approach implemented in this work for coupling the rigid body dynamics with the solution of the flow field proved to be very robust and yielded acceptable results. It also satisfies the requirement of working well for both steady and unsteady problems. To accurately simulate freely-floating body motions, no delay in the motion velocity is used, the correct moments of inertia have to be set and a better convergence at each time step is necessary. The implemented method has been successfully applied to the simulation of the dynamic responses of freely-floating bodies which are released from a position out of equilibrium. It has been validated for a 2-D test case for which experimental data exists: The asymmetrical drop test with a wedge. The comparison of simulated vertical and angular acceleration, impact velocity and angle of heel with the corresponding experimental data shows a surprisingly good agreement. The correct choice of Δt is very important to obtain the dynamic response. The effect of the number of outer iterations per time step is small compared to that of changing Δt. Unlike the experimental drop tests, the simulations deliver much more information at much lower cost and reduced delivery time.

The implemented method has also been applied to investigate the viscous roll damping of a 2-D boat section (with and without the keel), and of the full-scale boat at high forward speed. Viscous

effects are important for roll motion and should be taken into account to obtain realistic results. This approach can be used to perform roll extinction tests and sinusoidal roll excitation tests. The 2-D roll simulations showed that the approach is quite robust, since the free-surface sharpness automatically improves when a region of finer spacial resolution traverses the free surface, the top lid of the computational domain can dip into the water without causing numerical difficulties, and the mesh must not necessarily be restricted to a pre-determined roll angle range. The simulation of the coupled roll, pitch, sway and heave motion of large amplitude for the full scale boat sailing at high forward speed has been used to investigate the effects of Δt, outer iterations per time step and delay of motion velocity on the time needed for convergence towards the final running attitude as well as on the dynamic response. When only the final sailing attitude is looked for, the fastest convergence will be delivered by a large Δt, only one iteration per time step and a large delay of motion velocity. If the dynamic response is important, no delay can be used, at least five iterations and a Δt about five times smaller should be set. The CPU-time required for a time-accurate simulation of motions is at least four times larger than that for the calculation of the steady-state running attitude.

References

AZCUETA, R., (2001), *Computation of Turbulent Free-Surface Flows Around Ships and Floating Bodies*, PhD. thesis, Technical University Hamburg-Harburg (pdf file on request at rodrigo@azcueta.de).

AZCUETA, R. (2000), *Ship resistance prediction by free-surface RANS computations*, Ship Techn. Res. 47, pp.47-62

AZCUETA, R.; MUZAFERIJA, S.; PERIĆ, M. (1999a), *Computation of breaking bow waves for a very fat hull ship*, 7. Int. Conf. Num. Ship Hydrodyn., Nantes

AZCUETA, R.; MUZAFERIJA, S.; PERIĆ, M.; YOO, S. (1999b), *Computation of flows around hydrofoils under the free surface*, 7. Int. Conf. Num. Ship Hydrodyn., Nantes

BRANDT, H.; HOCHKIRCH, K.; ABDEL-MAKSOUD, M. (1997), *Leistungsanalysen für das Segeldynamometer*, Jahrbuch Schiffbautechn. Gesellschaft, Springer

CURA HOCHBAUM, A. (1998), *Computation of the turbulent flow around a ship model in steady turn and in steady oblique motion*, 22. Symp. Naval Hydrodyn., Washington, pp.198-213

LONGO, J.; STERN, F. (1996), *Yaw effects on model-scale ship flows*, 21. Symp. Naval Hydrodyn., Trondheim

MUZAFERIJA, S.; PERIĆ, M. (1998a), *Computation of free-surface flows using interface-tracking and interface-capturing methods*, Nonlinear Water Wave Interaction, Comp. Mech. Publ., pp.59-100

MUZAFERIJA, S.; PERIĆ, M.; SAMES, P.; SCHELLIN, T. (1998b), *A two-fluid Navier-Stokes solver to simulate water entry*, 22. Symp. Naval Hydrodyn., Washington

PETERSON, R.; WYMAN, D.; FRANK, C. (1997), *Drop tests to support water-impact and planing boat dynamics theory*, Techn. Rep. TR-97, Coastal Systems Station, Panama City

SAMES, P.C.; SCHELLIN, T.E.; MUZAFERIJA, S.; PERICĆ, M. (1998), *Application of a two-fluid finite volume method to ship slamming*, 17. Int. Conf. Offshore Mech. and Arctic Eng. (OMAE), Lisbon

SCHNEEKLUTH, H. (1988), *Hydromechanik zum Schiffsentwurf*, Koehler

SCHUMANN, C. (1998), *Volume-of-fluid computations of water entry of bow sections*, EUROMECH 374, Poitiers, pp.209-217

TROESCH, A.W.; KANG, C.G. (1990), *Evaluation of impact loads associated with flare slamming*, J. Soc. Naval Arch. Korea 27/3

XU, L.; TROESCH, A.W.; PETERSON, R. (1999), *Asymmetric hydrodynamic impact and dynamic response of vessels*, J. Offshore Mech. Arctic Eng. 121, pp.83-89

ZHAO, R.; FALTINSEN, O.M.; HASLUM, H. (1997), *A simplified nonlinear analysis of a high-speed planing craft in calm water*, FAST '97, Sydney, pp.431-437